American Mineralogist, Volume 107, pages xxx–xxx, 2022

An ab-initio study on the thermodynamics of disulfide, sulfide, and bisulfide incorporation into apatite and the development of a more comprehensive temperature, pressure, pH, and composition-dependent model for ionic substitution in minerals

Young Jae Kim[1,2,*,†], Brian Konecke[1,3], Adam Simon[1,‡], Adrian Fiege[1], and Udo Becker[1]

[1]University of Michigan, Department of Earth and Environmental Sciences, Ann Arbor, Michigan 48109, U.S.A.
[2]Chemical Sciences and Engineering Division, Argonne National Laboratory, Lemont, Illinois 60439, U.S.A.
[3]Fathom Geophysics, LLC, 12956 Claylick Road, Newark, Ohio 43056, U.S.A.

Abstract

The mineral apatite, $Ca_{10}(PO_4)_6(F,OH,Cl)_2$, incorporates sulfur (S) during crystallization from S-bearing hydrothermal fluids and silicate melts. Our previous studies of natural and experimental apatite demonstrate that the oxidation state of S in apatite varies systematically as a function of oxygen fugacity (f_{O_2}). The S oxidation states –1 and –2 were quantitatively identified in apatite crystallized from reduced, S-bearing hydrothermal fluids and silicate melts by using sulfur *K*-edge X-ray absorption near-edge structure spectroscopy (S-XANES) where $S^{6+}/\Sigma S$ in apatite increases from ~0 at FMQ-1 to ~1 at FMQ+2, where FMQ refers to the fayalite-magnetite-quartz f_{O_2} buffer. In this study, we employ quantum-mechanical calculations to investigate the atomistic structure and energetics of S(-I) and S(-II) incorporated into apatite and elucidate incorporation mechanisms.

One S(-I) species (disulfide, S_2^{2-}) and two S(-II) species (bisulfide, HS^-, and sulfide, S^{2-}) are investigated as possible forms of reduced S species in apatite. In configuration models for the simulation, these reduced S species are positioned along the *c*-axis channel, originally occupied by the column anions F, Cl, and OH in the end-member apatites. In the lowest-energy configurations of S-incorporated apatite, disulfide prefers to be positioned halfway between the mirror planes at $z = 1/4$ and 3/4. In contrast, the energy-optimized bisulfide is located slightly away from the mirror planes by ~0.04 fractional units in the *c* direction. The energetic stability of these reduced S species as a function of position along the *c*-axis can be explained by the geometric and electrostatic constraints of the Ca and O planes that constitute the *c*-axis channel.

The thermodynamics of incorporation of disulfide and bisulfide into apatite are evaluated by using solid-state reaction equations where the apatite host and a solid S-bearing source phase (pyrite and $Na_2S_{2(s)}$ for disulfide; troilite and $Na_2S_{(s)}$ for sulfide) are the reactants, and the S-incorporated apatite and an anion sink phase are the products. The Gibbs free energy (ΔG) is lower for incorporation with Na-bearing phases than with Fe-bearing phases, which is attributed to the higher energetic stability of the iron sulfide minerals as a source phase for S than the sodium sulfide phases. The thermodynamics of incorporation of reduced S are also evaluated by using reaction equations involving dissolved disulfide and sulfide species [$H_nS_{2(aq)}^{(2-n)}$ and $H_nS_{(aq)}^{(2-n)}$; n = 0, 1, and 2] as a source phase. The ΔG of S-incorporation increases for fluorapatite and chlorapatite and decreases for hydroxylapatite as these species are protonated (i.e., as n changes from 0 to 2). These thermodynamic results demonstrate that the presence of reduced S in apatite is primarily controlled by the chemistry of magmatic and hydrothermal systems where apatite forms (e.g., an abundance of Fe; solution pH). Ultimately, our methodology developed for evaluating the thermodynamics of S incorporation in apatite as a function of temperature, pH, and composition is highly applicable to predicting the trace and volatile element incorporation in minerals in a variety of geological systems. In addition to solid-solid and solid-liquid equilibria treated here at different temperatures and pH, the methodology can be easily extended also to different pressure conditions by just performing the quantum-mechanical calculations at elevated pressures.

Keywords: Sulfur incorporation into apatite, oxybarometer, disulfide, bisulfide, sulfide, fluorapatite, chlorapatite, hydroxylapatite, density functional theory (DFT) calculation; Experimental Halogens in Honor of Jim Webster

Introduction

The behavior of sulfur (S) in earth systems depends on temperature (*T*), pressure (*P*), **{{auth: note our style for pressue is italic *P*, fix elsewhere}}** oxygen (f_{O_2}), and sulfur (f_{S_2}) fugacity, and the composition (X) of the S-bearing fluid [i.e., hydrothermal or silicate melt (Carroll and Webster 2018; Webster et al. 2011)]. Sulfur is a polyvalent element that can coexist in multiple oxidation states (e.g., S^{6+}, S^{4+}, S^0, S^{1-}, and S^{2-}) and serves as an important ligand for the transportation and enrichment of metals (e.g., Cu, Fe, Ni, Ag, and Au) and critical elements (e.g., REEs)

* E-mail: youngjkm@umich.edu
† Special collection papers can be found online at http://www.minsocam.org/MSA/AmMin/special-collections.html.
‡ Orcid 0000-0002-1733-5718

in magmatic-hydrothermal and hydrothermal systems (Piccoli and Candela 2002; Simon and Ripley 2011; Wan et al. 2021). In silicate melts, sulfur is predominantly present as S^{6+} and/or S^{2-} (Baker and Moretti 2011; Jugo 2009; Jugo et al. 2010). However, previous studies have proposed intermediate oxidation states of sulfur (e.g., S^{4+}, S^0, and S^{1-}) that are stable in silicate melts (Matjuschkin et al. 2016; Métrich et al. 2009).

The S content at sulfide saturation (SCSS) and S content at sulfate saturation (SCAS) in silicate melts and hydrothermal fluids is controlled by *T-P-X* and the redox conditions of the system (Baker and Moretti 2011; Fiege et al. 2015; Jugo 2009; Keppler 1999; Kleinsasser et al. 2022; Simon and Ripley 2011; Zajacz et al. 2012). The S content in reduced silicate melts (f_{O_2} below ~FMQ, where FMQ refers to the fayalite-magnetite-quartz f_{O_2} buffer) is typically on the order of a few tens to a few hundred parts per million (ppm) of dissolved S as sulfide, whereas oxidized (f_{O_2} above ~FMQ +2) and water-rich silicate melt may contain up to 1.5 wt% S dissolved as sulfate (Jugo 2009; Jugo et al. 2005). The preservation of primary magmatic sulfate minerals (e.g., anhydrite) is rare in the volcanic rock record, because of the dissolution of anhydrite by meteoric water (Jakubowski et al. 2002; Luhr et al. 1984). For this reason, S-bearing minerals, where sulfate replaces major oxyanions in phosphate and silicate minerals, such as apatite and scapolite, are more common (Parat et al. 2011; Webster and Piccoli 2015). Since the S oxidation state is sensitive to the system f_{O_2}, the abundance of different oxidation states of S (i.e., $S^{6+}/\Sigma S$ where $\Sigma S = [S^{2-} + S^{1-} + S^{4+} + S^{6+}]$) in S-bearing minerals can serve as a proxy for the redox evolution of magmatic and magmatic-hydrothermal systems (Konecke et al. 2017, 2019).

Konecke et al. (2017, 2019) demonstrated experimentally that sulfur oxidation states in apatite, $Ca_{10}(PO_4)_6(F,OH,Cl)_2$, vary as a function of f_{O_2} in mafic melts. Specifically, the XANES data reported by those authors reveal that S^{2-} is the dominant oxidation state of S in igneous apatite equilibrated at FMQ while S^{6+} is predominant over S^{4+} and S^{2-} as f_{O_2} increases from FMQ+1.2 to FMQ+3. The data reported in those studies are the first to quantitatively demonstrate that apatite incorporates S oxidation states other than S^{6+} (in the form of sulfate), which has long been reported incorrectly to be the only possible redox state of S in natural apatite. Several studies have documented the presence of oxidation states of S other than, and in addition to, S^{6+} in natural apatite. Brounce et al. (2019) document the presence of S^{2-} in lunar apatite within samples 12039 and 10044, which are, respectively, a 3.2 ± 0.05 billion year old, low-TiO_2 basalt and a ~3.71–3.73 billion year old, high-TiO_2 basalt. Sadove et al. (2019) report the coexistence of multiple oxidation states of S (S^{6+}, S^{4+}, S^{1-}, and S^{2-}) in terrestrial apatite from the magnetite-sulfide mineral deposit at Phillips Mine, New York, U.S.A. Their work proposed that apatite grains with structurally incorporated reduced S species with oxidation states S^{1-} and S^{2-} crystallized initially from a reduced, S-bearing hydrothermal fluids, followed by secondary alteration (metasomatism) that resulted in the structural incorporation of oxidized S (i.e., S^{6+} and S^{4+}) in apatite. Tassara et al. (2020) document the presence of S^{2-} in apatite within basaltic tephra erupted from the Tashara Los Hornitos monogenetic cones in central-southern Chile, which are among the most primitive materials reported in the Southern Andes (olivine Mg# ≤ 92.5 and Ni ≤ 5000 ppm). Meng et al. (2021) **{{AU: 2021a or 2021b?}}** document the presence of S^{2-} in apatite from calc-alkaline plutonic rocks associated with the Haib porphyry Cu deposit in the Paleoproterozoic Richtersveld Magmatic Arc (southern Namibia), an interpreted mature island-arc setting. Meng et al. (2021) **{{AU: 2021a or 2021b?}}** document the presence of S^{2+} in primary apatite from tonalite-trondhejmite-granodiorite (TTG) igneous rocks temporally associated with the ~2.7 Ga St-Jude and Clifford porphyry-type Cu ± Au deposits in the Neoarchean southern Abitibi subprovince. In combination with the experimental results of Konecke et al. (2017, 2019), these data from natural terrestrial and lunar samples demonstrate that the $S^{6+}/\Sigma S$ ratio of apatite records the redox evolution of the melts and fluids from which it crystallized.

There is a dearth of data that constrain the substitution mechanisms for S species with different oxidation states in apatite. The presence of S^{6+} in natural apatite has been attributed to the substitution of SO_4^{2-} for PO_4^{3-} (Pan and Fleet 2002; Parat et al. 2011; Streck and Dilles 1998), whereas the presence of S^{2-} in apatite was only recently confirmed (e.g., Konecke et al. 2017, 2019; Sadove et al. 2019). Kim et al. (2017) computationally investigated thermodynamically plausible scenarios for the presence of S^{2-} in apatite that agree with the experimental observations reported by Konecke et al. (2017, 2019); e.g., $2(F,Cl,OH)^- \leftrightarrow S^{2-} + \square$. The results from Kim et al. (2017) demonstrated that S^{2-} behaves chemically like Cl^- in the *c*-axis channel of apatite and, therefore, can substitute for the column anions F^-, OH^-, and/or Cl^-. Those authors highlighted the need for future investigation of the substitution mechanisms for HS^- and other possible S species substitutions in apatite since they may occur in hydrothermal fluids when H_2S is deprotonated. The demonstrated presence of structurally bound S^{1-} and S^{2-} in natural apatite (Sadove et al. 2019) also highlights the need for a theoretical understanding of the incorporation mechanisms of reduced S species in apatite.

In this study, we apply and evaluate quantum-mechanical calculations to elucidate the energetics and geometry of reduced S species (oxidation state of –1 and –2) incorporated in the apatite structure. One S(-I) species, disulfide (S_2^{2-}), and two S(-II) species, bisulfide (HS^-) and sulfide (S^{2-}), are investigated as possible forms of reduced S in apatite. The following plausible substitution mechanisms were investigated: $2(F, Cl, OH)^- \leftrightarrow S_2^{2-} + \square$ (vacancy); $(F, Cl, OH)^- \leftrightarrow HS^-$; $2(F, Cl, OH)^- \leftrightarrow S^{2-} + \square$. This computational approach permits the determination of (1) the energetic favorability of S incorporation into apatite depending on the occupancy of the column anion and (2) the geometric and electrostatic constraints on the atomic site upon S incorporation. The results demonstrate the potential role of S-in-apatite as a proxy to trace redox conditions in magmatic and hydrothermal systems. This study builds on that of Kim et al. (2017), which was based on the molecular energies at 0 K, by including computationally expensive phonon analyses for the computation of enthalpy (including *cPT* terms) and Gibbs free energy contributions (including $-T\Delta S$ terms) for thermodynamics analyses. Both solids and aqueous species were included as a source and sink, which is a significant advancement in applying computational quantum-mechanical approaches to understanding the incorporation of redox-sensitive elements in minerals.

Methods

Computational parameters

Energy optimizations were performed using the quantum-mechanical code CASTEP (Segall et al. 2002). Computational constraints that successfully addressed

sulfur species with different oxidation states in apatite were adopted from Kim et al. (2017). While optimizations were applied to configurations of mineral structures, the cell parameters and atomic positions were subject to modification to achieve minimum energies of the systems. The computational code is based on density functional theory (DFT). The Perdew-Wang generalized gradient scheme (GGA) was used along with ultrasoft pseudopotentials and parameterized by the Perdew-Burke-Ernzerhof (PBE) functional (Perdew et al. 1996). The energy cutoff for planewave expansion was 400.0 eV, and the Brillouin zone was sampled using a k-point separation of 0.05 $Å^{-1}$ according to the Monkhorst-Pack scheme (Monkhorst and Pack 1976). The convergence tolerance for energy change was 2.0×10^{-6} eV/atom. The energy optimization yields the total electronic energy of a system at 0 K, which is termed molecular energy (E_{mol}) in this study.

The phonon density of state (DOS) was calculated using CASTEP after energy optimizations using norm-conserving pseudopotentials and the same convergence tolerance mentioned above. The linear response methodology was used with a convergence criterion of 1.0×10^{-5} eV/$Å^2$ for electronic eigenvalues and a k-point separation of 0.05 $Å^{-1}$. From the phonon DOS, the vibrational contributions to the Gibbs free energy (ΔG_{vib}) are evaluated for mineral species as the sum of the zero-point vibrational energy and the entropy correction (Baroni et al. 2001).

Incorporation energy calculations

Incorporation equations and energies of chemical species into a mineral are evaluated based on periodic solid-state reactions. The background and principles of this approach are discussed in detail in previous studies (Gebarski and Becker 2020; Kim et al. 2017; Reich and Becker 2006; Shuller-Nickles et al. 2014; Shuller et al. 2010; Walker and Becker 2015). Briefly, the general equation and energy are explained as follows.

$$\text{apatite}_{host} + \Sigma_{i=1}^{n} a_i\text{source}_i \leftrightarrow \text{apatite}_{S\text{-incorporated}} + \Sigma_{i=1}^{m} b_i\text{sink}_i \quad (1)$$

$$\Delta\Sigma_{rxn} = \Sigma E_{prod} - \Sigma E_{reac} \quad (2)$$

A host apatite phase (apatite_{host}) with any of the three common anions on the column anion site and sources for S (source_i) with different oxidation states are reactants, while S-incorporated apatite ($\text{apatite}_{S\text{-incorporated}}$) and sinks for anions being released from the apatite host (sink_i) are products. This approach allows for a consistent quantum-mechanical treatment, i.e., using the same computational parameters throughout the equation, which is crucial to obtain reliable energetic data. Once the molecular energies of all reactant and product phases are obtained from energy optimization, the reaction energy (ΔE_{mol}) for an incorporation reaction is calculated using Equation 2. This incorporation reaction energy indicates the stability of the S-incorporated apatite relative to the corresponding host apatite, as well as the source and sink phases. Furthermore, enthalpy (ΔH) and Gibbs free energy (ΔG) of selected incorporation reactions are evaluated at finite temperature (in this study, 25 °C and above) as the sum of total reaction energy (ΔE_{mol}), zero-point energy (ΔE_{zp}), and the vibrational contributions (ΔH_{vib} and ΔG_{vib}) obtained from energy optimizations and phonon analyses.

The thermodynamic data computed in this study were coupled with tabulated experimental thermodynamic data (standard state and 25 °C) to compare ΔG of incorporation reactions with various source and sink phases. The first step of this procedure is to estimate computationally ΔG of sulfur incorporation reactions into apatite (Tables 1 and 2) that involve Na-bearing source and sink phases (denoted as source_1 and sink_1 in Eq. 3). Among the source and sink phases examined in this study, Na-bearing phases were chosen for this thermodynamic evaluation (i.e., energy optimization followed by vibrational analysis) because they are computationally less demanding than Fe-bearing phases or sinks and sources of dissolved ions. However, the latter two options of sources and sinks (Fe-solids and aqueous reference species) were included by using thermodynamic data from the literature. In a geological context, reaction equations involving Na-bearing solid phases may represent model systems to simulate silicate melts where sodium is one of the major elements, and thus anions (like halide ions and reduced S species) may be present as bonded with sodium ions (Na^+). Experimental thermodynamic data (Online Materials[1] Table S1) were used to calculate a balanced equation of a reaction (Eq. 4) that relates the Na-bearing phases with a different kind of source and sink phase (denoted as source_2 and sink_2 in Eq. 4). By combining these two reaction equations (Eqs. 3 and 4), the reaction of S incorporation into apatite with source and sink phases of interest (Eq. 5) and its ΔG are obtained.

$$\text{apatite}_{host} + a_1\text{source}_1 \leftrightarrow a\text{patite}_{S\text{-incorporated}} + b_1\text{sink}_1 \quad (3)$$

$$a_1\text{source}_1 + b_2\text{sink}_2 \leftrightarrow a_2\text{source}_2 + b_1\text{sink}_1 \quad (4)$$

$$\text{apatite}_{host} + a_2\text{source}_2 \leftrightarrow \text{apatite}_{S\text{-incorporated}} + b_2\text{sink}_2 \quad (5)$$

For instance, a reaction equation of disulfide incorporation into fluorapatite involving Na-bearing source and sink phases is presented in Equation 6. The ΔG of this reaction is evaluated from energy optimization and phonon analysis. The ΔG of the reaction equation relating Na- and Fe-bearing phases (Eq. 7) is obtained from tabulated thermodynamic data (Online Materials[1] Table S1), and the ΔG of the incorporation reaction involving Fe-bearing phases is estimated by combining Equations 6 and 7.

TABLE 1. Reaction equations and energies of disulfide (S_2^{2-}) incorporation into apatite

Complete incorporation	Energy (kJ/mol)		
Na-bearing	ΔE_{mol}	ΔH	ΔG
$Ca_{10}(PO_4)_6F_{2(s)} + Na_2S_{2(s)} \leftrightarrow Ca_{10}(PO_4)_6S_{2(s)} + 2\ NaF_{(s)}$	108	155	128
$Ca_{10}(PO_4)_6Cl_{2(s)} + Na_2S_{2(s)} \leftrightarrow Ca_{10}(PO_4)_6S_{2(s)} + 2\ NaCl_{(s)}$	−22	−12	−16
$Ca_{10}(PO_4)_6OH_{2(s)} + Na_2S_{2(s)} \leftrightarrow Ca_{10}(PO_4)_6S_{2(s)} + 2\ NaOH_{(s)}$	157	175	173
Fe-bearing			ΔG
$Ca_{10}(PO_4)_6F_{2(s)} + FeS_{2(s)}$ (pyrite) $\leftrightarrow Ca_{10}(PO_4)_6S_{2(s)} + FeF_{2(s)}$			342
$Ca_{10}(PO_4)_6Cl_{2(s)} + FeS_{2(s)}$ (pyrite) $\leftrightarrow Ca_{10}(PO_4)_6S_{2(s)} + FeCl_{2(s)}$			239
$Ca_{10}(PO_4)_6OH_{2(s)} + FeS_{2(s)}$ (pyrite) $\leftrightarrow Ca_{10}(PO_4)_6S_{2(s)} + FeOH_{2(s)}$			234
Aqueous	ΔG (n = 0)	ΔG (n = 1)	ΔG (n = 2)
$Ca_{10}(PO_4)_6F_{2(s)} + H_nS_{2(aq)}^{(n-2)} \leftrightarrow Ca_{10}(PO_4)_6S_{2(s)} + n\ H^+ + 2\ F^-_{(aq)}$	199	244	273
$Ca_{10}(PO_4)_6F_{2(s)} + H_2S_{2(aq)} \leftrightarrow Ca_{10}(PO_4)_6S_{2(s)} + 2\ HF_{(aq)}$	–	–	237
$Ca_{10}(PO_4)_6Cl_{2(s)} + H_nS_{2(aq)}^{(n-2)} \leftrightarrow Ca_{10}(PO_4)_6S_{2(s)} + n\ H^+ + 2\ Cl^-_{(aq)}$	32	77	105
$Ca_{10}(PO_4)_6OH_{2(s)} + H_nS_{2(aq)}^{(n-2)} \leftrightarrow Ca_{10}(PO_4)_6S_{2(s)} + n\ H_2O_{(l)} + (2-n)\ OH^-_{(aq)}$	159	114	53
Partial incorporation	Energy (kJ/mol)		
Na-bearing	ΔE_{mol}	ΔH	ΔG
$2\ Ca_{10}(PO_4)_6F_{2(s)} + Na_2S_{2(s)} \leftrightarrow Ca_{20}(PO_4)_{12}F_2S_{2(s)} + 2\ NaF_{(s)}$	121	181	138
$2\ Ca_{10}(PO_4)_6Cl_2 + Na_2S_{2(s)} \leftrightarrow Ca_{20}(PO_4)_{12}Cl_2S_{2(s)} + 2\ NaCl_{(s)}$	−40	−56	−66
$2\ Ca_{10}(PO_4)_6OH_2 + Na_2S_{2(s)} \leftrightarrow Ca_{20}(PO_4)_{12}OH_2S_{2(s)} + 2\ NaOH_{(s)}$	164	175	164
Fe-bearing			ΔG
$2\ Ca_{10}(PO_4)_6F_{2(s)} + FeS_{2(s)}$ (pyrite) $\leftrightarrow Ca_{20}(PO_4)_{12}F_2S_{2(s)} + FeF_{2(s)}$			352
$2\ Ca_{10}(PO_4)_6Cl_2 + FeS_{2(s)}$ (pyrite) $\leftrightarrow Ca_{20}(PO_4)_{12}Cl_2S_{2(s)} + FeCl_{2(s)}$			188
$2\ Ca_{10}(PO_4)_6OH_2 + FeS_{2(s)}$ (pyrite) $\leftrightarrow Ca_{20}(PO_4)_{12}OH_2S_{2(s)} + FeOH_{2(s)}$			225
Aqueous	ΔG (n = 0)	ΔG (n = 1)	ΔG (n = 2)
$2\ Ca_{10}(PO_4)_6F_{2(s)} + H_nS_{2(aq)}^{(n-2)} \leftrightarrow Ca_{20}(PO_4)_{12}F_2S_{2(s)} + n\ H^+ + 2\ F^-_{(aq)}$	209	253	282
$2\ Ca_{10}(PO_4)_6F_{2(s)} + H_2S_{2(aq)} \leftrightarrow Ca_{20}(PO_4)_{12}F_2S_{2(s)} + 2\ HF_{(aq)}$	–	–	247
$2\ Ca_{10}(PO_4)_6Cl_{2(s)} + H_nS_{2(aq)}^{(n-2)} \leftrightarrow Ca_{20}(PO_4)_{12}Cl_2S_{2(s)} + n\ H^+ + 2\ Cl^-$(aq)	−18	27	55
$2\ Ca_{10}(PO_4)_6OH_{2(s)} + H_nS_{2(aq)}^{(n-2)} \leftrightarrow Ca_{20}(PO_4)_{12}OH_2S_{2(s)} + n\ H_2O_{(l)} + (2\text{-}n)\ OH^-_{(aq)}$	151	106	45

TABLE 2. Reactionequations and energies of sulfide (S^{2-}) and bisulfide (HS^{-}) incorporationinto apatite

Complete incorporation	Energy (kJ/mol)		
Na-bearing	ΔE_{mol}	ΔH	ΔG
Sulfide			
$Ca_{10}(PO_4)_6F_{2(s)} + Na_2S_{(s)} \leftrightarrow Ca_{10}(PO_4)_6S_{(s)} + 2NaF_{(s)}$	75	117	118
$Ca_{10}(PO_4)_6Cl_{2(s)} + Na_2S_{(s)} \leftrightarrow Ca_{10}(PO_4)_6S_{(s)} + 2NaCl_{(s)}$	−61	−70	−47
$Ca_{10}(PO_4)_6(OH)_{2(s)} + Na_2S_{(s)} \leftrightarrow Ca_{10}(PO_4)_6S_{(s)} + 2NaOH_{(s)}$	118	131	157
Bisulfide			
$Ca_{10}(PO_4)_6(OH)_{2(s)} + 2Na_2S_{(s)} \leftrightarrow Ca_{10}(PO_4)_6(HS)_{2(s)} + 2Na_2O_{(s)}$	494	514	476
$Ca_{10}(PO_4)_6(OH)_{2(s)} + 2NaSH_{(s)} \leftrightarrow Ca_{10}(PO_4)_6(HS)_{2(s)} + 2NaOH_{(s)}$	171	186	193
Fe-bearing			ΔG
Sulfide			
$Ca_{10}(PO_4)_6F_{2(s)} + FeS_{(s)}$ (troilite) $\leftrightarrow Ca_{10}(PO_4)_6S_{(s)} + FeF_{2(s)}$			285
$Ca_{10}(PO_4)_6Cl_{2(s)} + FeS_{(s)}$ (troilite) $\leftrightarrow Ca_{10}(PO_4)_6S_{(s)} + FeCl_{2(s)}$			160
Bisulfide			
$Ca_{10}(PO_4)_6(OH)_{2(s)} + 2FeS_{(s)}$ (troilite) $\leftrightarrow Ca_{10}(PO_4)_6(HS)_{2(s)} + 2FeO_{(s)}$ (wüstite)			208
Aqueous	ΔG (n= 0)	ΔG (n= 1)	ΔG (n = 2)
Sulfide			
$Ca_{10}(PO_4)_6F_{2(s)} + H_nS_{(aq)}^{(n-2)} \leftrightarrow Ca_{10}(PO_4)_6S_{(s)} + nH^+ + 2F_{(aq)}^-$	202	276	316
$Ca_{10}(PO_4)_6F_{2(s)} + H_2S_{(aq)} \leftrightarrow Ca_{10}(PO_4)_6S_{(s)} + 2HF_{(aq)}$			280
$Ca_{10}(PO_4)_6Cl_{2(s)} + H_nS_{(aq)}^{(n-2)} \leftrightarrow Ca_{10}(PO_4)_6S_{(s)} + nH^+ + 2Cl_{(aq)}^-$	14	88	127
Bisulfide			
$Ca_{10}(PO_4)_6OH_{2(s)} + 2H_nS_{(aq)}^{(n-2)} \leftrightarrow Ca_{10}(PO_4)_6(HS)_{2(s)} + 2H_nO_{(l)}^{(n-2)}$	–	171	72
Partial incorporation	Energy (kJ/mol)		
Na-bearing	ΔE_{mol}	ΔH	ΔG
Sulfide			
$2Ca_{10}(PO_4)_6F_{2(s)} + Na_2S_{(s)} \leftrightarrow Ca_{20}(PO_4)_{12}SF_{2(s)} + 2NaF_{(s)}$	185	247	209
$2Ca_{10}(PO_4)_6Cl_{2(s)} + Na_2S_{(s)} \leftrightarrow Ca_{20}(PO_4)_{12}SCl_{2(s)} + 2NaCl_{(s)}$	−69	−78	−92
$2Ca_{10}(PO_4)_6(OH)_{2(s)} + Na_2S_{(s)} \leftrightarrow Ca_{20}(PO_4)_{12}S(OH)_{2(s)} + 2NaOH_{(s)}$	244	253	260
Bisulfide			
$Ca_{10}(PO_4)_6OH_{2(s)} + Na_2S_{(s)} \leftrightarrow Ca_{10}(PO_4)_6(HS)OH_{(s)} + Na_2O_{(s)}$	246	241	227
$Ca_{10}(PO_4)_6OH_{2(s)} + NaSH_{(s)} \leftrightarrow Ca_{10}(PO_4)_6(HS)OH_{(s)} + NaOH_{(s)}$	86	89	79
Fe-bearing			ΔG
Sulfide			
$2Ca_{10}(PO_4)_6F_{2(s)} + FeS_{(s)}$ (troilite) $\leftrightarrow Ca_{20}(PO_4)_{12}SF_{2(s)} + FeF_{2(s)}$			376
$2Ca_{10}(PO_4)_6Cl_{2(s)} + FeS_{(s)}$ (troilite) $\leftrightarrow Ca_{20}(PO_4)_{12}SCl_{2(s)} + FeCl_{2(s)}$			114
Bisulfide			
$Ca_{10}(PO_4)_6OH_{2(s)} + FeS_{(s)}$ (troilite) $\leftrightarrow Ca_{10}(PO_4)_6(HS)OH_{(s)} + FeO_{(s)}$ (wüstite)			93
Aqueous	ΔG (n= 0)	ΔG (n= 1)	ΔG (n = 2)
Sulfide			
$2Ca_{10}(PO_4)_6F_{2(s)} + H_nS_{(aq)}^{(n-2)} \leftrightarrow Ca_{20}(PO_4)_{12}SF_{2(s)} + nH^+ + 2F_{(aq)}^-$	293	367	407
$2Ca_{10}(PO_4)_6F_{2(s)} + H_2S_{(aq)} \leftrightarrow Ca_{20}(PO_4)_{12}SF_{2(s)} + 2HF_{(aq)}$	–	–	371
$2Ca_{10}(PO_4)_6Cl_{2(s)} + H_nS_{(aq)}^{(n-2)} \leftrightarrow Ca_{20}(PO_4)_{12}SCl_{2(s)} + nH^+ + 2Cl_{(aq)}^-$	−32	42	82
Bisulfide			
$Ca_{10}(PO_4)_6OH_{2(s)} + H_nS_{(aq)}^{(n-2)} \leftrightarrow Ca_{10}(PO_4)_6(SH)(OH)_{(s)} + H_nO_{(l)}^{(n-2)}$	–	74	25

$$Ca_{10}(PO_4)_6F_{2(s)} = Na_2S_{2(s)} \leftrightarrow Ca_{10}(PO_4)_6S_{2(s)} + 2NaF_{(s)} \quad (\Delta G_{comp}^{incorp,Na}) \quad (6)$$

$$Na_2S_{2(s)} + FeF_{2(s)} \leftrightarrow 2NaF_{(s)} + FeS_{2(s)} \quad (\Delta G_{exp}^{Na,Fe}) \quad (7)$$

$$Ca_{10}(PO_4)_6F_{2(s)} + FeF_{2(s)} \leftrightarrow Ca_{10}(PO_4)_6S_{2(s)} + FeF_{2(s)}$$
$$(\Delta G_{combined}^{incorp,Fe} = \Delta G_{comp}^{incorp,Na} - \Delta G_{exp}^{Na,Fe}) \quad (8)$$

In the same manner, the ΔG of the incorporation reaction involving dissolved ionic species (Eq. 10) was estimated by using the equation relating Na-bearing phases and dissolved molecular species (Eq. 9).

$$Na_2S_{2(s)} + 2HF_{(aq)} \leftrightarrow 2NaF_{(s)} + H_2S_{2(aq)} \quad (\Delta G_{exp}^{Na,aq}) \quad (9)$$

$$Ca_{10}(PO_4)_6F_{2(s)} + H_2S_{2(aq)} \leftrightarrow Ca_{10}(PO_4)_6S_{2(s)} + 2HF_{(aq)}$$
$$(\Delta G_{combined}^{incorp,aq} = \Delta G_{comp}^{incorp,Na} - \Delta G_{exp}^{Na,aq}) \quad (10)$$

In essence, this approach combines incorporation energies that can be computed purely at the DFT level with the subsequent phonon calculations with experimental values for ΔG values of formation of different source and sink phases to make the transition between different systems. Applying this approach is particularly useful for evaluating the thermodynamics of incorporation reactions involving reactant and product phases that are geologically relevant but computationally demanding (in this study, Fe-bearing minerals and ions dissolved in aqueous solutions).

Structure models of apatite

The configuration models of the apatite end-members are adopted from the natural apatite structure, $[Ca_{10}(PO_4)_6(F,OH,Cl)_2]$ ($P6_3/m$; see Hughes et al. 1990; Hughes and Rakovan 2015) and are depicted in Figure 1. The apatite structure has two types of Ca sites, Ca1 and Ca2. The Ca1 site is coordinated to nine O atoms, while the Ca2 site is coordinated to six O atoms and one column anion (Figs. 1a and 1b). The three oxygen sites, O1, O2, and O3 in apatite, belong to the constituent phosphate, forming the four corners of the tetrahedra whose center is P^{5+}. The Ca2 and O3 triangular planes are aligned along the *c*-axis, forming the channel (Fig. 1c), and the sites within the *c*-axis channel [fractional coordinate = (0, 0, *z*)] are occupied by the main column anions, F^-, OH^-, and Cl^- (Fig. 1a). The planes in which the Ca2 triangles occur (also called the mirror planes) are located at $z = 1/4$ and 3/4 (Fig. 1a). The apatite end-members are subdivided into fluor-, hydroxyl-, and chlorapatite based on a single occupant of the anion column, but often occur in binary or ternary solid solution between/among the main column anions (Hughes et al. 1990; Hughes and Rakovan 2002). Thus, the *c*-axis channel has the potential to accommodate foreign anions with different radii and/or charges. One well-known example is carbonate (CO_3^{2-}) substituting for OH^- in hydroxylapatite (Fleet and Liu 2007), as it is common in bones and teeth and allows for greater flexibility to form a variety of morphologies.

Among the main column anions, fluorine is the smallest and located on the mirror planes at $z = 1/4$ and 3/4 at the center of the Ca triangle (Fig. 1a). Hydroxide and chlorine do not fit in the center of the Ca2 triangle and are thus displaced above or below the planes. There are multiple positions of OH^- and Cl^- along the *c*-axis channel (Hughes and Rakovan 2015). Since all atoms in apatite must be given full atomic occupancy for quantum-mechanical modeling, the OH^- and Cl^- positions below the planes at $z = 1/4$ and 3/4 were selected to complete the unit-cell formula, $[Ca_{10}(PO_4)_6(F,Cl,OH)_2]$ (Fig. 1a). Thus, the structures of hydroxyl- and chlorapatite reduce the symmetry to the $P6_3$ space group. Similar approaches to simulate hexagonal apatite without the *m* symmetry have been successfully tested in previous

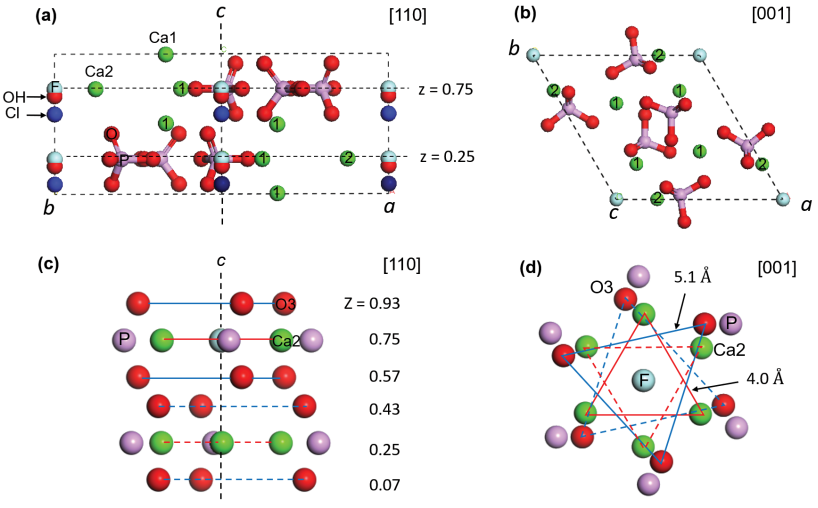

FIGURE 1. (**a** and **b**) The unit cell and (**c** and **d**) *c*-axis channel configurations of fluorapatite on view of [110] and [001] direction. In **a**, the relative positions (based on the *z* values; Online Materials[1] Table S2) of hydroxide and chloride are displayed in addition to fluorine. In **a** and **b**, the Ca atoms labeled 1 and 2 represent two types of Ca sites, Ca1 and Ca2. In **d**, the interatomic distances on each Ca2 and O3 plane are measured and used to estimate the channel sizes (see Fig. 7 and text for details). (Color online.)

computational studies (Corno et al. 2006; Ulian et al. 2013). Using the structural and computational parameters above, a good agreement in the unit-cell parameters was found between calculated and experimental end-member apatites reported by Hughes et al. (1989) (Online Materials[1] Table S2). The resulting structures are then used to energy-optimize the structure of the host and S-substituted apatite models.

It should be noted that in pure hydroxyl- and chlorapatite, the sense of ordering of hydroxide or chloride in any individual column (e.g., above or below the mirror plane) causes the adjacent column along the *b* axis to be ordered in the opposite direction (below or above the mirror plane) (Hughes et al. 1989; Hughes and Rakovan 2002). As a result, the symmetry of pure hydroxyl- and chlorapatite degenerates to $P2_1/b$ (Elliott et al. 1973; Mackie et al. 1972). Most natural hydroxyl and chlorapatite, however, are known to exist in the hexagonal space groups due to impurities or vacancies in the anion columns (Hughes and Rakovan 2002). In the apatite unit-cell and supercell models of this study, there is only one column along the c-axis and therefore, the alternating ordering of hydroxide and chloride between adjacent columns is not included in the energy-optimized structures. For this reason, the structural details of hydroxyl- and chlorapatite reported **{{auth: ok?}}**in this study are more representative of natural hexagonal apatite structures than pure monoclinic apatite structures.

Mechanisms of reduced S substitution

Although the major constituent column anions in apatite are F^-, OH^-, and Cl^-, various chemical substitutions can occur at the anion site in the *c*-axis channels of natural apatite. Pan and Fleet (2002) compiled examples of substituent ions and molecules in the *c*-axis channel that are monovalent, divalent, or neutral in charge and that can be monatomic, diatomic, or polyatomic. Here, we focus on possible forms and substitution mechanisms of reduced S species with oxidation states of -I and -II in apatite.

The first finding that S species can have an oxidation state of −1 in apatite was reported by Sadove et al. (2019). Possible forms of S(-I) include monovalent and monoatomic S (S^-; monoatomic sulfide) and divalent diatomic S (S_2^{2-}; disulfide) (Sadove et al. 2019). Since monoatomic sulfide has the same charge as the major column anions, simple substitution for F^-, OH^-, and Cl^- is possible at the column anion site (Eq. 6). Since disulfide is divalent and the column anion is monovalent in charge, the substitution of one disulfide for two column anions is needed to maintain the total charge neutral (Eq. 7).

$$(F,OH,Cl)^- \leftrightarrow S^- \quad (6)$$

$$2(F,OH,Cl)^- \leftrightarrow S_2^{2-} + \square \quad (7)$$

The presence of oxidation state S(-II) in apatite has been demonstrated experimentally (Konecke et al. 2017, 2019) and in natural samples (Sadove et al. 2019). As H_2S in a silicate melt or hydrothermal fluid is deprotonated, S(-II) species may be partitioned into mineral phases in the form of either bisulfide (HS^-) or sulfide (S^{2-}). Bisulfide can substitute for the column anion via simple substitution (Eq. 8) due to the same charges whereas substitution of one sulfide with two column anions (Eq. 9) is necessary for sulfide incorporation.

$$(F,OH,Cl)^- \leftrightarrow HS^- \quad (8)$$

$$2(F,OH,Cl)^- \leftrightarrow S^{2-} + \square \quad (9)$$

The structure model of S-substituted apatite

When the initial models (i.e., ones subjected to energy optimization) of sulfur-substituted apatite were built, F^-, OH^-, or Cl^- in the *c*-axis channel were replaced by reduced S species [S^- and S_2^{2-} for S(–I); S^{2-} and HS^- for S(-II)] in unit cells or supercells of fluor-, hydroxyl- and chlorapatite (based on Eqs. 6 to 9). During the process of energy optimization, the sulfide species can be repositioned to any unoccupied position of the column and then relax to local minima in the energy landscape. Therefore, in this study, it was examined whether there is an energetic or geometric variation in the optimization result with different initial positions of S^{2-} in the anion column. The position of F^-, Cl^-, and OH^- in the apatite anion column [i.e., (00z) obtained from energy-optimizing the end-member apatite structures; Online Materials[1] Table S2] was selected as the position of S species in the initial models, unless stated otherwise. Where necessary, S species at those positions are referred to as $S(X)_{ini}$ (where X = F, OH, or Cl). Here, complete incorporation is defined as S substitution wherein S is the only anion in the *c*-axis channel and partial incorporation is when S replaces some fraction (<1) of the column anions in the unit cell or supercell of apatite.

For S(-I) in apatite, the calculated molecular energy of two monoatomic sulfide ions (S^-) in the *c*-axis channel is 90 kJ/mol higher compared to that of one disulfide (S_2^{2-}) (compare Figs. 2a and 2c). This energy difference arises from the instability of monoatomic S^{-1} that has an unpaired electron (i.e., a radical species). Therefore, further investigation of geometry and reaction energy of S(-I) in apatite focuses on the incorporation of disulfide.

RESULTS

Energy-optimized structures

This section focuses on the energy-optimized structures of disulfide, bisulfide, and sulfide, replacing completely or partially the column anions in apatite. The optimization results indicate structural responses of fluor-, chlor-, and hydroxylapatite to accommodate these species (Online Materials[1] Table S3) and energetic stability of reduced S species (indicated by its total energy, E_{mol}) as a function of their position along the *c*-axis channel of apatite.

Disulfide (S_2^{2-})-incorporated apatite

Two possible models of complete incorporation of disulfide [$Ca_{10}(PO_4)_6(S_2)$] were built to examine the stability of apatite phases having disulfide aligned parallel to the *c*-axis channel

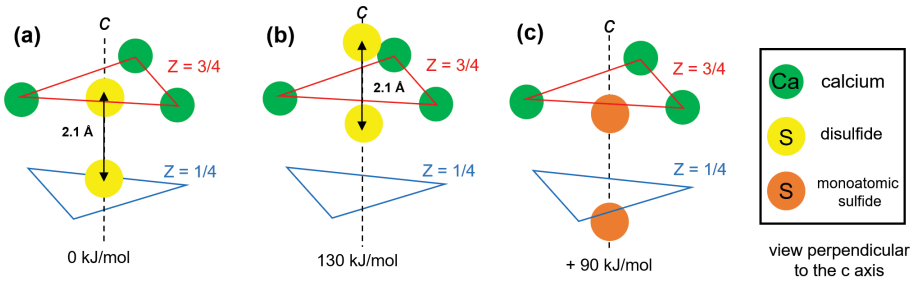

FIGURE 2. Energy-optimized geometries of S(-I) species in apatite. The configurations of disulfide with its center located at (**a**) $z = 1/2$ (halfway between the mirror planes at $z = 1/4$ and 3/4) and (**b**) $z = 3/4$. The distance of the two S atoms is 2.1 Å as acquired from energy-optimization. (**c**) The configuration of monoatomic S(-I) atoms located below the mirror plane at $z = 1/4$ and 3/4. While all these configuration models represent the same composition of S-incorporated apatite, $[Ca_{10}(PO_4)_6S_2]$, the lowest molecular energy is found in the configuration described in **a**. The energy values are with respect to this lowest-energy configuration. (Color online.)

(Fig. 2). One model is that disulfide is positioned halfway between the Ca2 triangular planes (Fig. 2a). In the other model, the center of disulfide is located on the mirror plane at $z = 1/4$ or 3/4 (Fig. 2b). From energy-optimization, the former model is 130 kJ/mol (in E_{mol}) more stable than the latter one (Fig. 3a). In the energy-optimized structure of the former model, the two S atoms of disulfide are located at (0,0,0.66) and (0,0,0.35), and the S-S distance in disulfide is 2.1 Å (Fig. 3a). This S-S bond length of disulfide in apatite is in good agreement with the molecular geometry of hydrogen disulfide (H_2S_2) (Dixon et al. 1985). The cell parameters of disulfide-incorporated apatite are listed in Online Materials[1] Table S3. The unit cells of disulfide-incorporated apatite are 2 to 6% longer in lattice parameters *a* and *b* and < 2% shorter in parameter *c* relative to their respective host apatite, fluor-, chlor-, and hydroxylapatite.

Nine possible models of partial incorporation, in the form of $[Ca_{20}(PO_4)_{12}(S_2)(F,OH,Cl)_2]$ examine the atomic structure of disulfide interacting with neighboring column anions in the *c*-axis channel (Fig. 4). The initial models (the ones prior to energy optimization) were built using 1 × 1 × 2 supercells of apatite in which the *z* value (with respect to the original unit cell) of the anion in the *c*-axis channel ranges between 0 and 2. In the initial models, column anions, F^-, OH^-, and Cl^-, are positioned on or below the mirror plane at $z = 7/4$ and 1/4, while the centers of the respective disulfide units are located at $z = 1/2$, 3/4, and 1. The energy-optimized structures of the nine possible models show that disulfide initially positioned at $z = 1/2$ and 3/4 (Figs. 4b and 4c) moves to $z \approx 1$ or remains near $z \approx 1/2$ while the major column anions move away. One reason for this repositioning of the anions in the *c*-axis channel is repulsion between disulfide and the column anions. In the optimized structure, disulfide is located halfway between the neighboring column anions such that the repulsion between disulfide and the column anion is minimized. In addition, it is energetically unfavorable for disulfide to be located on the mirror planes at $z = 3/4$ (Fig. 4c) because its stability is lower than when positioned between the mirror planes, as demonstrated from the calculations on the complete incorporation of disulfide (Fig. 2).

Overall, the simulation results of complete and partial incorporation of disulfide predict that disulfide is most energetically stable halfway between the mirror planes at $z = 1/4$ and 3/4 in the unit cell of apatite.

Bisulfide (HS^-)-incorporated apatite

In the models of bisulfide replacing column anions entirely, $Ca_{10}(PO_4)_6(HS)_2$, bisulfide that is initially positioned at the F site remains on the mirror planes at $z = 1/4$ and 3/4 (equivalent to the F site in apatite) while HS^- initially placed at the OH and Cl site is displaced from the mirror plane by 0.04 in the *z* direction, which corresponds to the OH site in hydroxylapatite (Fig. 3b). The calculated E_{mol} of complete incorporation of bisulfide is nearly the same (the difference ≈ 2 kJ/mol) for HS^- occupying the OH and F sites (Fig. 3b). The cell parameters of bisulfide-incorporated apatite are listed in Online Materials[1] Table S3. For lattice parameter *a*, the unit cells of bisulfide-incorporated apatite are 1 to 5% larger than the host apatite ones. The deviation of lattice parameter *c* from the host apatite is <2%.

Nine possible models of bisulfide partial incorporation, in the form of $Ca_{10}(PO_4)_6(HS)(F,OH,Cl)$, examine bisulfide in apatite that interacts with neighboring column anions (Fig. 5). In the initial models, bisulfide occupies the column anion sites on or below the mirror plane at $z = 3/4$, while the neighboring F, OH, and Cl, are on or below the mirror plane at $z = 1/4$. Like complete incorporation of bisulfide, the most favorable configurations of partially incorporated bisulfide are close to the F and OH sites ($z = 0.68$ to 0.76)

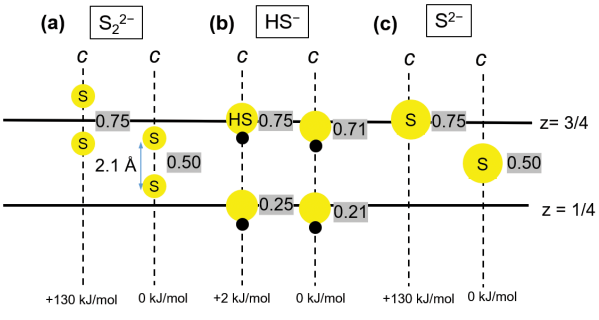

FIGURE 3. Energy-optimized structures of complete incorporation of (**a**) disulfide, (**b**) bisulfide, and (**c**) sulfide into apatite. The two solid lines represent the mirror planes in apatite at $z = 1/4$ and 3/4. The *z* values (gray highlighted) are specified to indicate the positions of the center of disulfide in **a** and the positions of S atoms belonging to bisulfide and sulfide in **b** and **c**. The energy values are with respect to the lowest energy calculated for respective species in apatite. (Color online.)

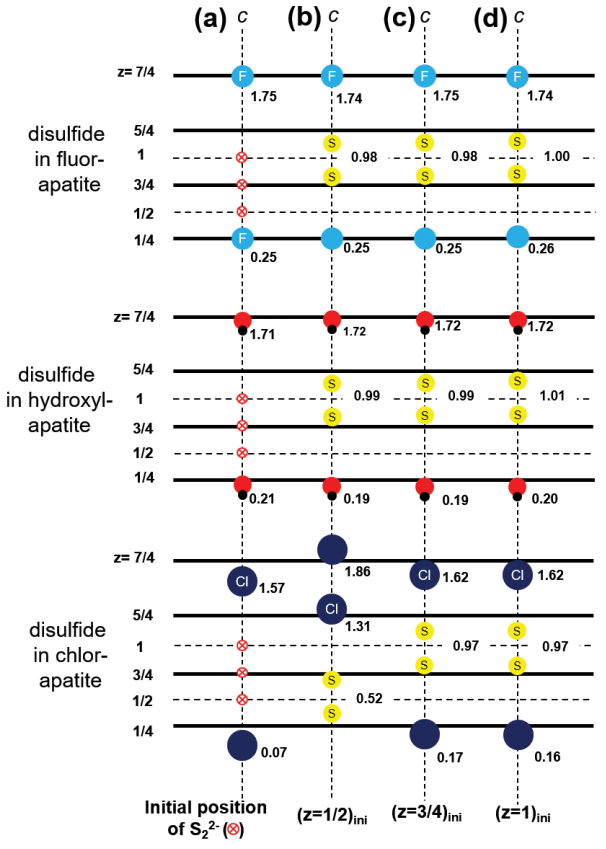

FIGURE 4. (**a**) Initial and (**b** to **d**) energy-optimized configurations (i.e., ones before and after the process of energy optimization) for partial incorporation of disulfide in the *c*-axis column anion channel in the form of $[Ca_{20}(PO_4)_{12}(S_2)(F,OH,Cl)_2]$. The *z* value (with respect to the unit cell) of the anions in the *c*-axis channel ranges between 0 and 2. In the initial configurations, the center of disulfide was positioned at (**b**) $z = 1/2$, (**c**) $z = 3/4$, and (**d**) $z = 1$. (Color online.)

(Fig. 5). During energy optimization, the *z* positions of neighboring F and OH change by less than 0.02 fractional unit, whereas the Cl position ($z = 0.07$ in chlorapatite; Fig. 5a) is shifted in the *z* direction toward the mirror plane by 0.08 to 0.11 fractional units (Figs. 5b–5d). The shifted positions of chlorine indicate that the electrostatic interaction between the column anion and bisulfide is repulsive such that the column anion moves away from bisulfide.

Sulfide (S^{2-})-incorporated apatite

Previous modeling work by Kim et al. (2017) investigated the complete and partial incorporation of sulfide into the *c*-axis channel in apatite using the same computational procedure as the present study. Here, a brief synopsis of their relevant results is provided.

In the complete incorporation model with the chemical formula of $[Ca_{10}(PO_4)_6S]$, incorporation of sulfide (S^{2-}) occurs at $z = 1/2$. This atomic position of sulfide in apatite is in good agreement with experimental data for sulfoapatite (Henning et al. 2000). The calculated E_{mol} of sulfide-incorporated apatite was found to be 130 kJ/mol lower for the unit cell of apatite having sulfide at $z = 1/2$ than at $z = 3/4$ (equivalent to the F site in fluorapatite). This result indicates that it is energetically unfavorable to accommodate sulfide on the F site in apatite.

The partial incorporation of sulfide into apatite was examined using nine possible configuration models with stoichiometry $[Ca_{20}(PO_4)_{12}(S)(F,OH,Cl)_2]$ [see Fig. 5 in Kim et al. (2017)]. The energy optimization results showed that sulfide in apatite is most energetically stable when positioned at $z = 0.51$ to 0.61, which is close to the Cl site in natural apatite (displacement by 0.18 in *z* value from the mirror planes). Like disulfide and bisulfide in apatite (Figs. 4 and 5), it was found that neighboring F, Cl, and OH were shifted from their original positions in the *c*-axis channel due to repulsive interaction between the column anion and sulfide.

Thermodynamics of reduced S incorporation into apatite

The thermodynamics of disulfide, bisulfide, and sulfide incorporation into apatite were evaluated for the reaction equations involving Na-bearing solids, Fe-bearing solids, and species dissolved in aqueous solution as source and sink phases (Tables 1 and 2). For the reactions involving Na-bearing phases, we calculated all three thermodynamic entities, ΔE_{mol}, ΔH, and ΔG. While ΔE_{mol} is the sum of the core-core, core-electron, and electron interaction in the system in addition to the kinetic energy of the electrons (i.e., the "*E*" in the Schrödinger equation $H\Psi = E\Psi$ at 0 K), ΔH contains the zero-point vibrational energy (ZPE) and *cPT*, and ΔG contains the ZPE, *cPT*, and the vibrational entropy term $-T\Delta S$. ΔG and ΔH values are derived using a quasi-harmonic vibrational analysis at 25 °C and also at higher temperatures, as described below. The energetic properties (ΔE_{mol}, ΔH, and ΔG) of the equations involving Na-bearing phases are computationally obtained, while the ΔG

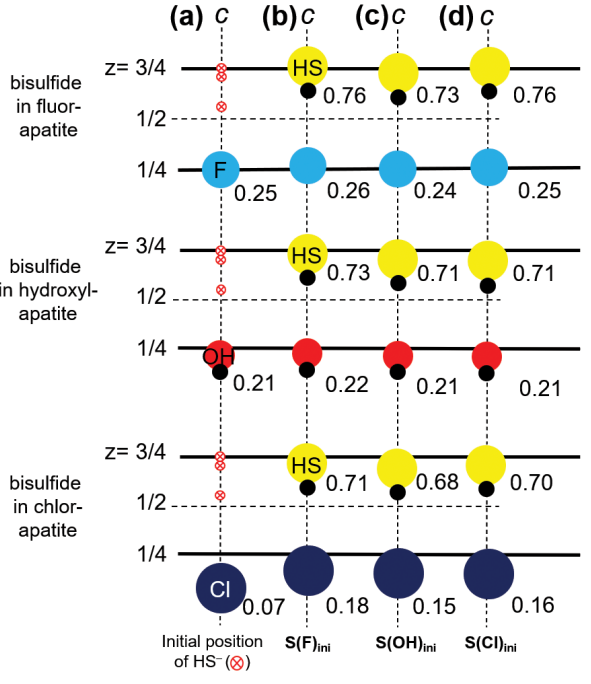

FIGURE 5. (**a**) Initial and (**b** to **d**) energy-optimized configurations for partial incorporation of bisulfide in the *c*-axis channel of apatite in the form of $[Ca_{10}(PO_4)_6(HS)(F,OH,Cl)]$. In the initial configurations, bisulfide was positioned at the (**b**) fluorine, (**c**) hydroxide, and (**d**) chlorine sites in the *c*-axis channel [denoted by $S(F,OH,Cl)_{ini}$]. (Color online.)

of equations involving Fe-bearing phases and dissolved species are evaluated by combining the computed data with tabulated experimental thermodynamic data (Online Materials[1] Table S1) for "pure" (non-incorporated) source and sink phases (see Methods section for details). The ΔG values of incorporation depend highly on selected source and sink phases; this is not an artifact, as different source phases represent thermodynamically stable minerals or solid compounds in different geochemical environments. These thermodynamic data provide insights into physicochemical parameters controlling the incorporation of reduced S species into apatite in geological systems (see Discussion section).

Disulfide incorporation into apatite

The reaction equations and energies for complete and partial incorporation of disulfide into apatite are presented in Table 1. There is a trend of Na-bearing phases that the enthalpy of incorporation is higher than the molecular energy by 10 to 60 kJ/mol. Then, the entropy of the reaction increases such that ΔG is less positive for fluor- and hydroxylapatite and more negative for chlorapatite than ΔH. For the same Na-bearing, Fe-bearing, and aqueous source and sink phases, the differences in ΔG between complete and partial incorporation reactions are less than 60 kJ/mol.

In the reactions involving Na-bearing phases, the ΔE_{mol}, ΔH, and ΔG of disulfide incorporation is lowest for chlorapatite, followed by fluorapatite and hydroxylapatite. Complete substitution (i.e., replacement) of Cl by disulfide is about 144 kJ/mol more favorable than replacement of F and 189 kJ/mol more favorable than replacement of OH. These energy differences are accounted for by the following reaction equations:

$$Ca_{10}(PO_4)_6F_{2(s)} + 2NaCl_{(s)} \leftrightarrow Ca_{10}(PO_4)_6Cl_{2(s)} + 2NaF_{(s)} \quad (10)$$

$$Ca_{10}(PO_4)_6(OH)_{2(s)} + 2NaCl_{(s)} \leftrightarrow Ca_{10}(PO_4)_6Cl_{2(s)} + 2NaOH_{(s)} \quad (11)$$

From the experimental thermodynamic data [Online Materials[1] Table S1b; Drouet (2015)], the ΔG of Equations 10 and 11 are evaluated to be 90 kJ/mol (±97 kJ/mol) and 135 kJ/mol (±81 kJ/mol), which are comparable with our DFT-calculated ΔG, 144 and 189 kJ/mol, respectively. The uncertainties of these experimental ΔG values are equivalent to the standard deviation of the Gibbs free energy of formation (ΔG^0_f) values of fluor-, chlor- and hydroxylapatite as compiled from previous studies (Drouet 2015 and references therein).

In the reactions involving Fe-bearing phases, the ΔG of incorporation is lower for chlorapatite and hydroxylapatite than for fluorapatite, which is in part because of the higher stability of $Fe(OH)_{2(s)}$ as the sink phase than $FeF_{2(s)}$ and $FeCl_{2(s)}$. In general, the Gibbs free energies of the reactions involving Na-bearing phases (−70 to 170 kJ/mol) are lower than those involving Fe-bearing phases (190 to 350 kJ/mol). This outcome arises from the thermodynamic stability of pyrite as a source phase for disulfide relative to $Na_2S_{2(s)}$.

For the treatment of hydrothermal source and sink phases, we considered dissolved molecular species as the source and sink phases (Table 1). $H_2S_{2(aq)}$, $HS^-_{2(aq)}$, and $S^{2-}_{2(aq)}$ (on the reactant side) were used as source phases for disulfide and $HF_{(aq)}$, $F^-_{(aq)}$, $Cl^-_{(aq)}$, and $OH^-_{(aq)}$, $H_2O_{(l)}$ (on the product side) were used as sink phases for the column anions. The protonation states of disulfide and fluoride species change as a function of pH, and their speciation diagrams are presented in Online Materials[1] Figure S1 (hydrochloric acid is always deprotonated). pK_{a1} and pK_{a2} of $H_2S_{2(aq)}$ are 5.0 and 9.7 and pK_{a1} of $HF_{(aq)}$ is 3.1. It follows that at pH below 5.0, $H_2S_{2(aq)}$ is the most dominant disulfide species, while both $HF_{(aq)}$ and $F^-_{(aq)}$ can exist in this pH range. At pH above 5.0, $HS^-_{2(aq)}$ becomes dominant [$S^{2-}_{2(aq)}$ at pH > 10], and F^- is the major fluoride species (Online Materials[1] Fig. S1). Considering these variations in speciation with pH, four possible reaction equations of disulfide incorporation with $HF_{(aq)}$ and $F^-_{(aq)}$ as the sink phase, three reaction equations with Cl^-, and three reaction equations with $OH^-_{(aq)}$ and $H_2O_{(l)}$ are balanced, and their Gibbs free energies are evaluated (Table 1). Overall, the ΔG values for both complete and partial incorporation are lower for chlor- and hydroxylapatite than for fluorapatite. Furthermore, by linearly combining these reaction equations with protonated and deprotonated species, we evaluate the ΔG of incorporation involving dissolved source and sink phases at equilibrium molar fractions that vary as a function of pH (Figs. 6a and 6b). For both complete and partial incorporation, ΔG decreases with pH for incorporation into fluor- and chlorapatite but increases with pH for hydroxylapatite. Among the three host apatite phases, the ΔG of complete and partial incorporation is lowest for hydroxylapatite at pH below 4 and for chlorapatite at pH above 5.

Bisulfide incorporation into apatite

The reaction equations and energies of complete and partial incorporation of bisulfide into hydroxylapatite are presented in Table 2. The ΔG is 476 kJ/mol for complete incorporation and 227 kJ/mol for partial incorporation when $Na_2S_{(s)}$ and $Na_2O_{(s)}$ are source and sink. The ΔG of reactions involving $NaSH_{(s)}$ and $NaOH_{(s)}$ is 193 kJ/mol for complete incorporation and 79 kJ/mol for partial incorporation. The ΔG of incorporation with Fe-bearing phases is 208 and 93 kJ/mol for complete and partial incorporation, respectively. The differences in Gibbs free energy between the reactions involving different source and sink phases are attributed to the energetic instability of $Na_2O_{(s)}$ as the sink phase relative to $NaOH_{(s)}$ and wüstite (FeO). For the incorporation reactions involving molecular species dissolved in aqueous solutions, the ΔG of incorporation with $H_2S_{(aq)}$ and $H_2O_{(l)}$ as the source and sink phases is 72 for complete incorporation and 25 kJ/mol for partial incorporation. The ΔG of incorporation involving $HS^-_{(aq)}$ and $OH^-_{(aq)}$ is 171 and 74 kJ/mol for complete and partial incorporation, respectively. The dependence of ΔG of incorporation on the protonation states of the source and sink phases originates from the higher acidity of $H_2S_{(aq)}$ than $H_2O_{(l)}$ (pK_{a1} of H_2S is 5.0 and pK_a of H_2O is 15.7; Online Materials[1] Table S1e).

Sulfide incorporation into apatite

The reaction equations and energies of complete and partial incorporation of sulfide into fluor-, hydroxyl-, and chlorapatite are presented in Table 2. In the reactions involving Na-bearing phases, the Gibbs free energy is lower for incorporation of sulfide into chlorapatite than that into fluor- and hydroxylapatite. For incorporation into fluorapatite, the Gibbs free energy of partial incorporation (209 kJ/mol) is about 90 kJ/mol higher than that of complete incorporation, whereas the Gibbs free energy of partial incorporation into chlorapatite (−92 kJ/mol) is 45 kJ/mol lower than that of complete incorporation. This is in part because struc-

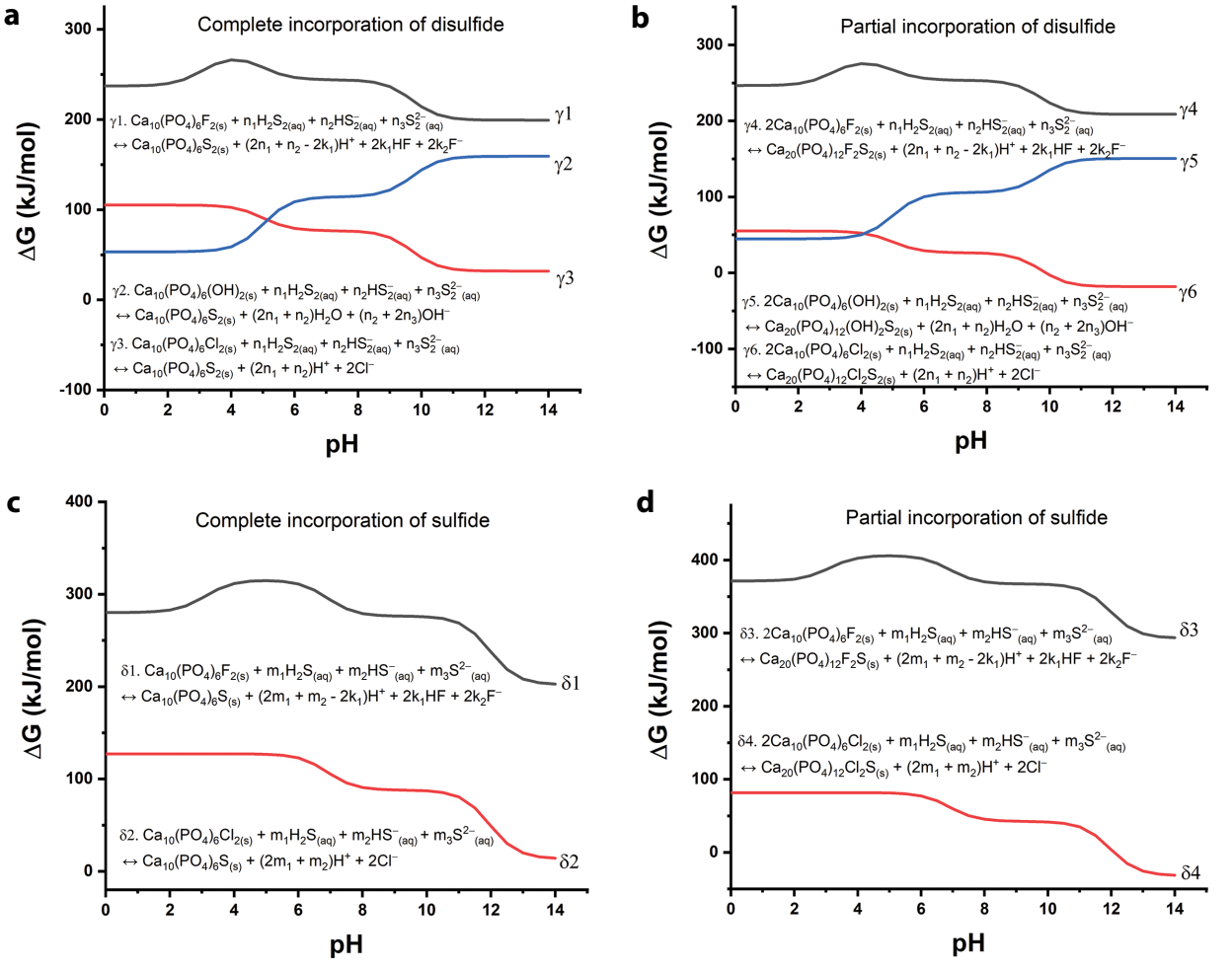

FIGURE 6. Gibbs free energy (ΔG) is calculated as a function of pH, assuming thermodynamic equilibrium at 25 °C, for (**a** and **b**) complete and partial incorporation of disulfide and (**c** and **d**) complete and partial incorporation of sulfide into apatite using source and sink phases dissolved in aqueous solution. The fractions of dissolved disulfide species, H_2S_2, HS_2^-, and S_2^{2-} (n_1, n_2, and n_3, respectively, where $n_1 + n_2 + n_3 = 1$), sulfide species, H_2S, HS^-, and S^{2-} (m_1, m_2, and m_3, respectively, where $m_1 + m_2 + m_3 = 1$), and` F species, HF and F^- (k_1 and k_2, respectively, where $k_1 + k_2 = 1$) vary as a function of pH as presented in Online Materials[1] Figure S1. These pH dependences of dissolved S and F species are considered to balance the reaction equations. (Color online.)

tural distortion (indicated by a change in cell parameters; Online Materials[1] Table S3) occurs to a lesser extent for accommodating sulfide in chlorapatite than in fluorapatite. The Gibbs free energies of reaction involving Fe-bearing phases are higher than those involving Na-bearing phases by 170 kJ/mol for incorporation into fluorapatite and by 210 kJ/mol for incorporation into chlorapatite. These differences in Gibbs free energy come from the higher stability of troilite (FeS) as the source phase (on the reactant side) compared to that of $Na_2S_{(s)}$.

In the reaction equations of incorporation involving dissolved molecular species (Table 2), $H_2S_{(aq)}$, $HS^-_{(aq)}$, and $S^{2-}_{(aq)}$ (on the reactant side) are used as source phases for sulfide and $HF_{(aq)}$, $F^-_{(aq)}$, $Cl^-_{(aq)}$, $H^+_{(aq)}$, $OH^-_{(aq)}$, and $H_2O_{(l)}$ (on the product side) as sink phases for the column anions. At pH below 6.9, $H_2S_{(aq)}$ is the most dominant among the sulfide species, while both $HF_{(aq)}$ and $F^-_{(aq)}$ can exist in this pH range (Online Materials[1] Fig. S1). At pH above 6.9, $HS^-_{(aq)}$ and $S^{2-}_{(aq)}$ become dominant and $F^-_{(aq)}$ is the major fluoride species. Like incorporation of disulfide, considering these variations in speciation with pH, four possible reaction equations of disulfide incorporation with $HF_{(aq)}$ and $F^-_{(aq)}$ as the sink phase and three reaction equations with $Cl^-_{(aq)}$ are balanced, and their Gibbs free energies are evaluated (Table 2). Overall, the ΔG of sulfide incorporation with the same aqueous source phases is lower for chlorapatite than for fluorapatite by 150–190 kJ/mol for complete incorporation and by 290–330 kJ/mol for partial incorporation (Table 2). From the linear combination of these reaction equations with protonated and deprotonated species, we calculate the ΔG of incorporation reactions in an aqueous environment with varying pH (Figs. 6c and 6d). For both complete and partial incorporation, ΔG decreases with pH for incorporation into fluor- and chlorapatite. This result indicates that the incorporation of sulfide into apatite is thermodynamically more favorable under alkaline conditions than neutral and acidic conditions.

Discussion

The stability of S species in the *c*-axis column channel

The modeling results of this study and Kim et al. (2017) demonstrate that the stability of reduced S species (S_2^{2-}, HS^-, and S^{2-}) in apatite depends highly on the atomic sites that the sulfide species occupy. In the energy-optimized configurations of S-incorporated apatite, disulfide prefers to occupy the positions halfway between the mirror planes at z = 1/4 and 3/4 (Figs. 3a and 4), whereas bisulfide is positioned slightly away (~0.04 in z value) from or on the mirror planes (Figs. 3b and 5). Sulfide is most energetically stable when close to the Cl site in apatite (Kim et al. 2017). In this section, some theoretical considerations are discussed to explain how the energetic stability of the incorporated S species depends on the geometry and the constituent elements (Ca and O atoms; Figs. 1c and 1d) of the *c*-axis channel.

The *c*-axis channel comprises O3 and Ca2 triangular planes perpendicular to the *c*-axis (Figs. 1c and 1d). Since the size and the electric charge (i.e., positively charged Ca vs. negatively charged O planes) of the *c*-axis channel are changed with z, the position of a substituent ion that occupies the *c*-axis channel can be determined by: (1) electrostatic interaction of the substituent anion with the Ca2 and O3 triangular planes and (2) the geometric constraint in the *c*-axis channel. The electrostatic contribution is due to attractive and repulsive interactions between the Ca2/O3 plane and the substituent ion. Geometrically, substitution is likely to occur if the channel and the substituent ion are similar in size.

The first step to quantify these constraints on a substituent ion in the *c*-axis channel is to estimate the size of the *c*-axis channel of apatite as a function of z. We postulate that the channel geometry is approximated by a series of circles along the *c*-axis tangent to the Ca2 and O3 triangular planes (Fig. 7a). The interatomic distances between calcium atoms on the Ca2 plane and O atoms on the O3 plane range from 4.0 to 4.4 and from 5.0 to 5.5 Å, respectively, depending on the occupant of the column anion site (Online Materials[1] Table S4). In the structure of fluor-, chlor-, and hydroxylapatite, the estimated channel radii on the Ca2 planes range between 1.3 and 1.5 Å and the O3 planes between 1.6 to 1.9 Å (Online Materials[1] Table S4; Fig. 7b).

Based on the estimated geometry of the *c*-axis channel, we examined whether the calculated position of reduced S species, S_2^{2-}, HS^-, and S^{2-} in the *c*-axis channel is consistent with the geometric and electrostatic constraints described above. Our calculation shows that disulfide in the *c*-axis channel is the most energetically stable when its center is located halfway between the mirror plane at z = 1/4 and 3/4 (Figs. 3a and 4). This geometry enables disulfide to maximize attractive interaction with the positively charged Ca planes at z = 1/4 and 3/4 (electrostatic contribution), while the two O3 planes at z = 0.57 and 0.43 have more spacious channels than the Ca2 planes (Fig. 7b) to accommodate disulfide molecules (geometric contribution). For bisulfide in apatite, the approximate size of HS^- (≈1.4 Å, the S-H distance of HS^-) falls within a range of the channel radii of the Ca2 planes (1.3 and 1.5 Å; Fig. 7b). The difference in electronegativity between sulfur and hydrogen generates the partial negative charge near sulfur and the partial positive charge near hydrogen. The oxygen in the O3 planes attracts the hydrogen of HS^- whereas the hydrogen repels the calcium in the Ca2 plane. Therefore, the calculated position of the S atom of HS^- being slightly away from the mirror plane by ~0.04 in z value (Fig. 3b) is explained by considering the geometric and electrostatic constraints. In the energy-optimized structures of sulfide-incorporated apatite reported by Kim et al. (2017), sulfide (S^{2-}) in apatite is displaced away from the mirror planes by 1.0 to 1.6 Å, which corresponds to the atomic sites near to the O3 planes at z = 0.57 and 0.43 (≈ the Cl site in chlorapatite). Since the ionic radius of sulfide (1.84 Å; Shannon 1976) exceeds the channel radius of the Ca2 planes, it is energetically stable when it is accommodated in wider channels around the O3 planes (Fig. 7b). Overall, the positions of reduced S species in apatite calculated from our modeling approaches are in good agreement with the geometric and electrostatic constraints of the *c*-axis column anion channel. These examples of reduced S species demonstrate that the geometric and electrostatic considerations on the *c*-axis channel can be useful in predicting the behavior of chemical species incorporated in apatite.

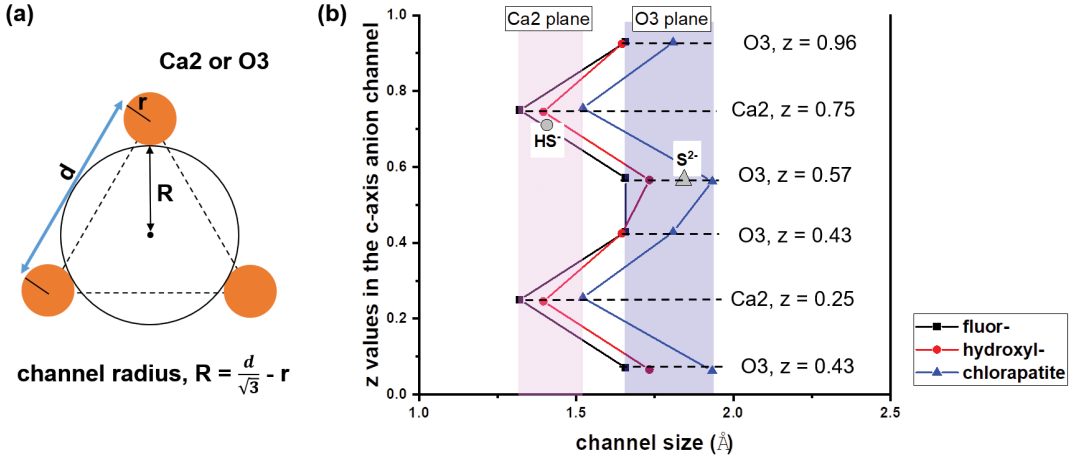

Figure 7. (**a**) The scheme to estimate the radius of the c-axis channel on the Ca2 and O3 planes in the apatite unit cell and (**b**) the variation in the radius of the *c*-axis anion channel of fluor-, hydroxyl-, and chlorapatite across the *c*-axis. In **b**, the ionic radii of the substituent ions (HS^- and S^{2-}) and their energy-optimized positions in the *c*-axis channel are plotted with the gray symbols. (Color online.)

Parameters controlling the thermodynamics of reduced S in apatite in geological systems

In the computational approach of this study, the thermodynamics of disulfide, bisulfide, and sulfide incorporation are evaluated using different source and sink phases (Tables 1 and 2). In general, the calculated energy of incorporation is lower for the reactions involving Na-bearing phases than those involving Fe-bearing phases (like pyrite and troilite on the reactant side). These results arise from the higher stability of these iron sulfide minerals as the source phase for S compared to sodium sulfide phases. In turn, it is inferred that when S-incorporated apatite occurs in association with sulfide minerals, the presence of reduced S species in apatite are primarily controlled by the chemistry of a system where apatite forms (e.g., Fe-abundant vs. depleted). This inference is consistent with Sadove et al. (2019), who reported the presence of inclusions of pyrrhotite and pyrite in natural S-incorporated apatite from the Phillip magnetite-sulfide mineral deposit (New York). Their data demonstrated that reduced S species were partitioned between iron sulfide and apatite as those phases crystallized from a reduced, S-bearing hydrothermal fluid.

Our computed data also indicate that the speciation of dissolved S species would be important in controlling the thermodynamics of incorporation reactions in aqueous media. For reactions with fluor- and chlorapatite as the host phases, incorporation of disulfide and sulfide in deprotonated forms like S_2^{2-} and S^{2-} is more thermodynamically favorable than incorporation in protonated forms. In contrast, protonation of sulfide increases the thermodynamic favorability of disulfide and bisulfide incorporation into hydroxylapatite. These computational results demonstrate that the form of S species incorporated in apatite (e.g., sulfide vs. bisulfide) could be determined by fluid pH where apatite forms through aqueous processes (like low-temperature aqueous and hydrothermal systems).

Temperature is another crucial parameter in controlling the thermodynamics of S incorporation in geological environments such as magmatic and hydrothermal systems. To demonstrate the effect of temperature on thermodynamics, the Gibbs free energy of complete and partial incorporation of disulfide with Na-bearing and Fe-bearing phases as a function of temperature is evaluated using temperature-dependent ΔG values of incorporation (Fig. 8). For

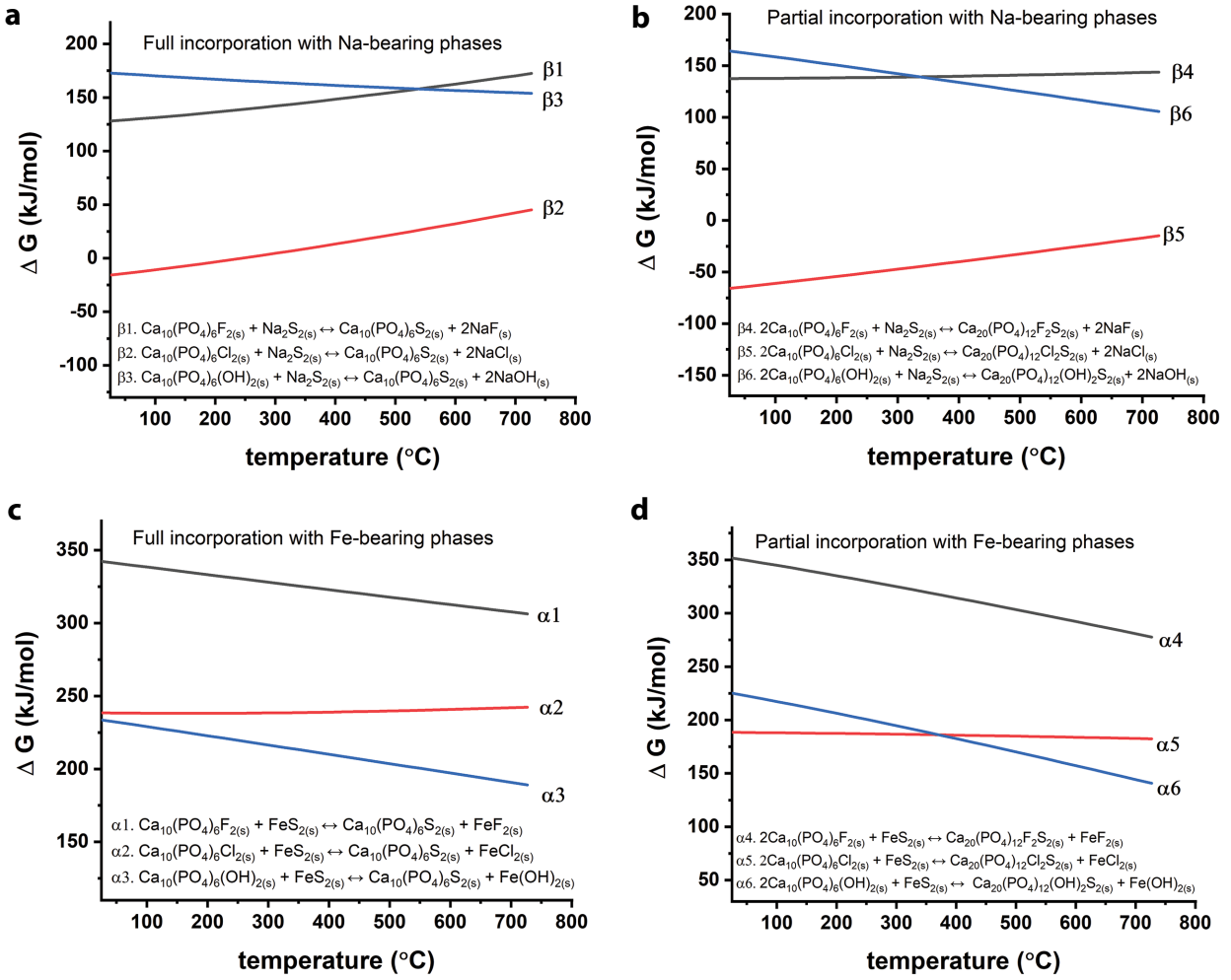

Figure 8. Gibbs free energy (ΔG) as a function of temperature for complete and partial incorporation of disulfide with (**a** and **b**) Na-bearing and (**c** and **d**) Fe-bearing source and sink phases. (Color online.)

Na-bearing systems, the ΔG of disulfide incorporation increases with temperature for fluor- and chlorapatite but decreases with increasing temperature for hydroxylapatite. For Fe-bearing systems, the ΔG of disulfide incorporation into fluor- and hydroxylapatite decreases, and that into chlorapatite increases as temperature increases. Our computed thermodynamic data suggest that the thermodynamic favorability of S incorporation into apatite is likely to be temperature-dependent in geological systems. At elevated temperatures, there may be thermodynamic advantages when disulfide is incorporated into fluor- and chlorapatite in Fe-enriched environments and into hydroxylapatite in Fe-depleted conditions.

Our methodology that combines DFT-computed thermodynamic data with experimental thermodynamic data has been demonstrated to have the potential for evaluating the thermodynamics of S incorporation in apatite in various geological systems. The thermodynamic data obtained from this approach can be used to predict the partitioning of reduced S species between apatite and other S-bearing minerals (in this study, pyrite and troilite) under varying temperature, pH, and composition. Our new approach opens up the possibility of using DFT modeling to establish the thermodynamic basis to support experimental and field observations on element incorporation in minerals and to understand the underlying mechanism and thermodynamics in more detail. In addition, it can inspire experimentalists for further evaluation. For example, the calculations presented here indicate a strong preference for chlorapatite to incorporate different S species than the other two host apatites, which should be easily verifiable by experiments. In general, the full quantum-mechanical derivation of the thermodynamics of an incorporation reaction is time-consuming, especially the Gibbs free energy portion that requires phonon analysis, which can be an order of magnitude more computationally expensive than the molecular energy E_{mol} only. However, once the Gibbs free energies of related source and sink phases are available, in solid or aqueous form, the transition to such a different reference model is a matter of minutes. This step can then be taken further relatively easily to geochemical mixtures.

It would be important to examine sources of errors in both the experimental and the computational portion of this approach. As stated in one example above, applying Gibbs free energies of formation from different literature studies can result in uncertainties of at least tens of kJ/mol, making a critical evaluation of thermodynamic data necessary. The error in the calculations is of a different nature. One caveat of calculations is that complete error analysis is often more expensive than the calculation itself if the entire space of potential errors is scanned, them either being computational parameters (DFT functional, basis functions, k-point density, pseudopotentials, or higher-order effects for heavy elements such as spin-orbit coupling or relativistic effects) or model setup (the most notable one, here, is the unit-cell size). Fortunately, some of these effects cancel out because they may be similar on both sides of a given equation, especially if oxidation states do not change across the equation.

In this study, we have evaluated the incorporation thermodynamics as a function of speciation, temperature, and for some examples of aqueous source/sink phases, pH. Another variable that is rather straightforward to modify is pressure. However, the derivation of thermodynamics becomes very demanding at high temperatures when simulating reactions in melts or hydrothermal solutions. Some questions that one would have to address are: Are solid reference phases still a viable approximation, or do they break down or even lose their internal structure (melt)? Is the quasi-harmonic phonon approximation still holding true for phonon calculations? How are solubility products and pK_a values defined in hydrothermal solutions of high *P-T*?

Implications

This study addresses the structural incorporation of reduced S species with the S(-II) and S(-I) oxidation states into apatite and the response of the apatite structure to these substituents. Other than sulfide (S^{2-}) that can substitute for column anions in the *c*-axis channel (Henning et al. 2000; Kim et al. 2017), bisulfide (HS^-) is another potential form of sulfur species with oxidation state S(-II) in apatite via simple substitution of $HS^- \leftrightarrow (F, OH, Cl)^-$. Of the two simplest S(-I) species, disulfide (S_2^{2-}) is the energetically more stable and plausible form in apatite than monoatomic sulfide (S^-). In general, the energetic stability and crystallographic characteristics of the S species in the *c*-axis channel of apatite vary depending on the S oxidation state and chemical forms (S_2^{2-}, HS^-, and S^{2-}) and can be affected by: (1) the neighboring column anion (F^-, OH^-, or Cl^-) and (2) geometric and electrostatic constraints by the Ca2 and O3 planes along the *c*-axis.

The presence of volatile elements (especially halogens, sulfur, and carbon) in apatite is ubiquitous in igneous and hydrothermal environments (Webster and Piccoli 2015). Although, historically, S^{6+} has been considered the most dominant oxidation state of sulfur in natural apatite [cf. Parat et al. (2011)], recent studies have demonstrated the strong dependence of the S oxidation state in apatite as a function of oxygen fugacity (f_{O_2}) and the formation of apatite containing variable proportions of S^{6+}, S^{4+}, S^{1-}, and S^{2-} as crystallized from magmatic and hydrothermal fluids (Konecke et al. 2017, 2019; Sadove et al. 2019). In line with these previous studies, the modeling of different S species in the apatite structure in this study implies that the oxidation state of S in apatite has the potential to serve as a geochemical proxy to probe the f_{O_2} and f_{S_2} of magmatic and hydrothermal systems.

Funding

Y.K. acknowledges support from Samsung Scholarship. A.C.S. acknowledges the U.S. National Science Foundation EAR 1924142.

References cited

Baker, D.R., and Moretti, R. (2011) Modeling the solubility of sulfur in magmas: A 50-year old geochemical challenge. Reviews in Mineralogy and Geochemistry, 73, 167–213.

Baroni, S., De Gironcoli, S., Dal Corso, A., and Giannozzi, P. (2001) Phonons and related crystal properties from density-functional perturbation theory. Reviews of Modern Physics, 73, 515 –562.

Brounce, M., Boyce, J., McCubbin, F.M., Humphreys, J., Reppart, J., Stolper, E., and Eiler, J. (2019) The oxidation state of sulfur in lunar apatite. American Mineralogist, 104, 307–312.

Carroll, M.R., and Webster, J.D. (2018) Solubilities of sulfur, noble gases, nitrogen, chlorine, and fluorine in magmas. Volatiles in Magmas, 231–280.

Corno, M., Busco, C., Civalleri, B., and Ugliengo, P. (2006) Periodic ab initio study of structural and vibrational features of hexagonal hydroxyapatite $Ca_{10}(PO_4)_6(OH)_2$. Physical Chemistry Chemical Physics, 8, 2464–2472.

Dean, J.A. (1990) Lange's Handbook of Chemistry. Material and manufacturing process, 5(4), 687–688. McGraw-Hill.

Dixon, D.A., Zeroka, D.J., Wendoloski, J.J., and Wasserman, Z.R. (1985) The molecular structure of hydrogen disulfide (H_2S_2) and barriers to internal rotation. The Journal of Physical Chemistry, 89, 5334–5336.

Drouet, C. (2015) A comprehensive guide to experimental and predicted thermodynamic

properties of phosphate apatite minerals in view of applicative purposes. The Journal of Chemical Thermodynamics, 81, 143–159.
Elliott, J.C., Mackie, P., and Young, R. (1973) Monoclinic hydroxyapatite. Science, 180, 1055–1057.
Fiege, A., Holtz, F., Behrens, H., Mandeville, C.W., Shimizu, N., Crede, L.S., and Göttlicher, J. (2015) Experimental investigation of the S and S-isotope distribution between H_2O–S±Cl fluids and basaltic melts during decompression. Chemical Geology, 393-394, 36–54.
Fleet, M.E., and Liu, X. (2007) Coupled substitution of type A and B carbonate in sodium-bearing apatite. Biomaterials, 28, 916–926.
Gebarski, B.B., and Becker, U. (2020) Quantum-mechanical determination of the incorporation of pentavalent plutonium into carbonate and sulfate minerals. Geochimica et Cosmochimica Acta, 269, 693–710.
Henning, P.A., Adolfsson, E., and Grins, J. (2000) The chalcogenide phosphate apatites $Ca_{10}(PO_4)_6S$, $Sr_{10}(PO_4)_6S$, $Ba_{10}(PO_4)_6S$ and $Ca_{10}(PO_4)_6Se$. Zeitschrift für Kristallographie—Crystalline Materials, 215, 226–230.
Hughes, J.M., and Rakovan, J. (2002) The crystal structure of apatite, $Ca_5(PO_4)_3(F,OH,Cl)$. Reviews in Mineralogy and Geochemistry, 48, 1–12.
——— (2015) Structurally robust, chemically diverse: apatite and apatite supergroup minerals. Elements, 11, 165–170.
Hughes, J.M., Cameron, M., and Crowley, K.D. (1989) Structural variations in natural F, OH, and Cl apatites. 74, 870–876.
——— (1990) Crystal structures of natural ternary apatites; solid solution in the $Ca_5(PO_4)_3X$ (X= F, OH, Cl) system. American Mineralogist, 75, 295–304.
Jakubowski, R.T., Fournelle, J., Welch, S., Swope, R., and Camus, P. (2002) Evidence for magmatic vapor deposition of anhydrite prior to the 1991 climactic eruption of Mount Pinatubo, Philippines. American Mineralogist, 87, 1029–1045.
Jordan, J. (1979) Instrumental analysis of sulfur compounds in coal process streams. Quarterly technical progess report, January-March 1979. Pennsylvania State University, University Park.
Jugo, P.J. (2009) Sulfur content at sulfide saturation in oxidized magmas. Geology, 37, 415–418.
Jugo, P.J., Luth, R.W., and Richards, J.P. (2005) Experimental data on the speciation of sulfur as a function of oxygen fugacity in basaltic melts. Geochimica et Cosmochimica Acta, 69, 497–503.
Jugo, P.J., Wilke, M., and Botcharnikov, R.E. (2010) Sulfur *K*-edge XANES analysis of natural and synthetic basaltic glasses: Implications for S speciation and S content as function of oxygen fugacity. Geochimica et Cosmochimica Acta, 74, 5926–5938.
Keppler, H. (1999) Experimental evidence for the source of excess sulfur in explosive volcanic eruptions. Science, 284, 1652–1654.
Kim, Y., Konecke, B., Fiege, A., Simon, A., and Becker, U. (2017) An ab-initio study of the energetics and geometry of sulfide, sulfite, and sulfate incorporation into apatite: The thermodynamic basis for using this system as an oxybarometer. American Mineralogist, 102, 1646–1656.
Kleinsasser, J.M., Simon, A.C., Konecke, B.A., Kleinsasser, M.J., Beckmann, P., and Holtz, F. (2022) Sulfide and sulfate saturation of dacitic melts as a function of oxygen fugacity. Geochimica et Cosmochimica Acta, 326, 1–16.
Konecke, B.A., Fiege, A., Simon, A.C., Parat, F., and Stechern, A. (2017) Co-variability of S^{6+}, S^{4+}, and S^{2-} in apatite as a function of oxidation state: Implications for a new oxybarometer. American Mineralogist, 102, 548–557.
Konecke, B.A., Fiege, A., Simon, A.C., Linsler, S., and Holtz, F. (2019) An experimental calibration of a sulfur-in-apatite oxybarometer for mafic systems. Geochimica et Cosmochimica Acta, 265, 242–258.
Kumagai, Y., and Abiko, Y. (2017) Environmental electrophiles: protein adducts, modulation of redox signaling, and interaction with persulfides/polysulfides. Chemical Research in Toxicology, 30(1), 203–219.
Luhr, J.F., Carmichael, I.S., and Varekamp, J.C. (1984) The 1982 eruptions of El Chichón Volcano, Chiapas, Mexico: Mineralogy and petrology of the anhydritebearing pumices. Journal of Volcanology and Geothermal Research, 23, 69–108.
Mackie, P., Elliot, J., and Young, R. (1972) Monoclinic structure of synthetic $Ca_5(PO_4)_3Cl$, chlorapatite. Acta Crystallographica, B28, 1840–1848.
Matjuschkin, V., Blundy, J.D., and Brooker, R.A. (2016) The effect of pressure on sulphur speciation in mid-to deep-crustal arc magmas and implications for the formation of porphyry copper deposits. Contributions to Mineralogy and Petrology, 171, 1–25.
Meng, X., Kleinsasser, J.M., Richards, J.P., Tapster, S.R., Jugo, P.J., Simon, A.C., Kontak, D.J., Robb, L., Bybee, G.M., Marsh, J.H., and Stern, R.A. (2021a) Oxidized sulfur-rich arc magmas formed porphyry Cu deposits by 1.88 Ga. Nature Communications, 12, 1–9.
Meng, X., Richards, J.P., Kontak, D.J., Simon, A.C., Kleinsasser, J.M., Marsh, J.H., Stern, R.A., and Jugo, P.J. (2021b) Variable modes of formation for tonalite-trondhjemite-granodiorite-diorite (TTG)-related porphyry-type Cu±Au deposits in the Neoarchean southern Abitibi subprovince (Canada): Evidence from petrochronology and oxybarometry. Journal of Petrology, 62.
Métrich, N., Berry, A.J., O'Neill, H.St.C., and Susini, J. (2009) The oxidation state of sulfur in synthetic and natural glasses determined by X-ray absorption spectroscopy. Geochimica et Cosmochimica Acta, 73, 2382–2399..
Monkhorst, H.J., and Pack, J.D. (1976) Special points for Brillouin-zone integrations. Physical Review B, 13, 5188–5192.
Pan, Y., and Fleet, M.E. (2002) Compositions of the apatite-group minerals: substitution mechanisms and controlling factors. Reviews in Mineralogy and Geochemistry, 48, 13–49.
Parat, F., Holtz, F., and Streck, M.J. (2011) Sulfur-bearing magmatic accessory minerals. Reviews in Mineralogy and Geochemistry, 73, 285–314.
Perdew, J.P., Burke, K., and Ernzerhof, M. (1996) Generalized gradient approximation made simple. Physical Review Letters, 77, 3865–3868.
Piccoli, P.M., and Candela, P.A. (2002) Apatite in igneous systems. Reviews in Mineralogy and Geochemistry, 48, 255–292.
Reich, M., and Becker, U. (2006) First-principles calculations of the thermodynamic mixing properties of arsenic incorporation into pyrite and marcasite. Chemical Geology, 225, 278–290.
Sadove, G., Konecke, B.A., Fiege, A., and Simon, A.C. (2019) Structurally bound S^{2-}, S^{1-}, S^{4+}, S^{6+} in terrestrial apatite: The redox evolution of hydrothermal fluids at the Phillips mine, New York, U.S.A. Ore Geology Reviews, 107, 1084–1096.
Segall, M., Lindan, P.J., Probert, MA., Pickard, C.J., Hasnip, P.J., Clark, S., and Payne, M. (2002) First-principles simulation: ideas, illustrations and the CASTEP code. Journal of Physics: Condensed Matter, 14, 2717.
Shannon, R. (1976) Revised effective ionic radii and systematic studies of interatomic distances in halides and chalcogenides. Acta Crystallographica, A32, 751–767.
Shuller, L.C., Ewing, R.C., and Becker, U. (2010) Quantum-mechanical evaluation of Np-incorporation into studtite. American Mineralogist, 95, 1151–1160.
Shuller-Nickles, L.C., Bender, W.M., Walker, S.M., and Becker, U. (2014) Quantum-mechanical methods for quantifying incorporation of contaminants in proximal minerals. Minerals. Minerals, 4, 690–715.
Simon, A.C., and Ripley, E.M. (2011) The role of magmatic sulfur in the formation of ore deposits. Reviews in Mineralogy and Geochemistry, 73, 513–578.
Streck, M.J., and Dilles, J.H. (1998) Sulfur evolution of oxidized arc magmas as recorded in apatite from a porphyry copper batholith. Geology, 26, 523–526.
Tassara, S., Reich, M., Konecke, B.A., González-Jiménez, J.M., Simon, A.C., Morata, D., Barra, F., Fiege, A., Schilling, M.E., and Corgne, A. (2020) Unraveling the effects of melt–mantle interactions on the gold fertility of magmas. Frontiers in Earth Science, 8, 29.
Ulian, G., Valdrè, G., Corno, M., and Ugliengo, P. (2013) Periodic ab initio bulk investigation of hydroxylapatite and type A carbonated apatite with both pseudopotential and all-electron basis sets for calcium atoms. American Mineralogist, 98, 410–416.
Walker, S.M., and Becker, U. (2015) Uranyl (VI) and neptunyl (V) incorporation in carbonate and sulfate minerals: Insight from first-principles. Geochimica et Cosmochimica Acta, 161, 19–35.
Wan, Y., Wang, X., Chou, I.-M., and Li, X. (2021) Role of sulfate in the transport and enrichment of REE in hydrothermal systems. Earth and Planetary Science Letters, 569, 117068.
Webster, J.D., and Piccoli, P.M. (2015) Magmatic apatite: A powerful, yet deceptive, mineral. Elements, 11, 177–182.
Webster, J.D., Goldoff, B., and Shimizu, N. (2011) C-O-H-S fluids and granitic magma: how S partitions and modifies CO_2 concentrations of fluid-saturated felsic melt at 200 MPa. Contributions to Mineralogy and Petrology, 162, 849–865.
Zajacz, Z., Candela, P.A., Piccoli, P.M., Wälle, M., and Sanchez-Valle, C. (2012) Gold and copper in volatile saturated mafic to intermediate magmas: Solubilities, partitioning, and implications for ore deposit formation. Geochimica et Cosmochimica Acta, 91, 140–159.

Manuscript received August 14, 2021
Manuscript accepted November 23, 2021
Manuscript handled by Justin Filiberto

Endnote:

[1]Deposit item AM-22-118250, Online Materials. Deposit items are free to all readers and found on the MSA website, via the specific issue's Table of Contents (go to http://www.minsocam.org/MSA/AmMin/TOC/2022/Nov2022_data/Nov2022_data.html).